Since January 2020 Elsevier has created a COVID-19 resource centre with free information in English and Mandarin on the novel coronavirus COVID-19. The COVID-19 resource centre is hosted on Elsevier Connect, the company's public news and information website.

Science of the Total Environment 812 (2022) 152592

Contents lists available at ScienceDirect

Science of the Total Environment

journal homepage: www.elsevier.com/locate/scitotenv

A spatiotemporally resolved infection risk model for airborne transmission of COVID-19 variants in indoor spaces

Xiangdong Li [a], Daniel Lester [a,*,1], Gary Rosengarten [a], Craig Aboltins [b], Milan Patel [a], Ivan Cole [a]

[a] School of Engineering, RMIT University, Melbourne, VIC 3000, Australia
[b] Department of Infectious Diseases, Northern Health, Epping, VIC 3076, Australia

HIGHLIGHTS

- A tempo-spatially resolved predictive model for COVID-19 infection is developed.
- A theoretical frame integrating engineering designs and clinical data is proposed.
- The application of the model to a typical hospital ward is demonstrated.

GRAPHICAL ABSTRACT

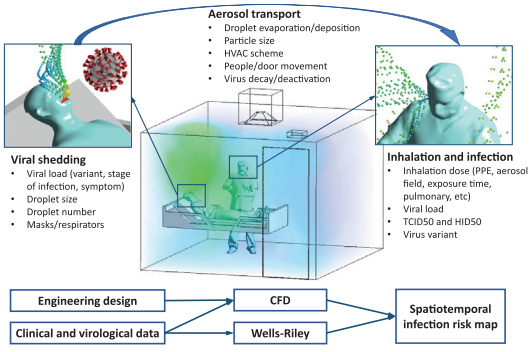

ARTICLE INFO

Article history:
Received 23 September 2021
Received in revised form 15 December 2021
Accepted 17 December 2021
Available online 23 December 2021

Editor: Pavlos Kassomenos

Keywords:
SARS-CoV-2
Covid-19
Delta variant
Wells-Riley model
Spatiotemporal infection risk

ABSTRACT

The classic Wells-Riley model is widely used for estimation of the transmission risk of airborne pathogens in indoor spaces. However, the predictive capability of this zero-dimensional model is limited as it does not resolve the highly heterogeneous spatiotemporal distribution of airborne pathogens, and the infection risk is poorly quantified for many pathogens. In this study we address these shortcomings by developing a novel spatiotemporally resolved Wells-Riley model for prediction of the transmission risk of different COVID-19 variants in indoor environments. This modelling framework properly accounts for airborne infection risk by incorporating the latest clinical data regarding viral shedding by COVID-19 patients and SARS-CoV-2 infecting human cells. The spatiotemporal distribution of airborne pathogens is determined via computational fluid dynamics (CFD) simulations of airflow and aerosol transport, leading to an integrated model of infection risk associated with the exposure to SARS-CoV-2, which can produce quantitative 3D infection risk map for a specific SARS-CoV-2 variant in a given indoor space. Application of this model to airborne COVID-19 transmission within a hospital ward demonstrates the impact of different virus variants and respiratory PPE upon transmission risk. With the emergence of highly contagious SARS-CoV-2 variants such as the Delta and Omicron strains, respiratory PPE alone may not provide effective protection. These findings suggest a combination of optimal ventilation and respiratory PPE must be developed to effectively control the transmission of COVID-19 in healthcare settings and indoor spaces in general. This generalised risk estimation framework has the flexibility to incorporate further clinical data as such becomes available, and can be readily applied to consider a wide range of factors that impact transmission risk, including location and movement of infectious persons, virus variant and stage of infection, level of PPE and vaccination of infectious and susceptible individuals, impacts of coughing, sneezing, talking and breathing, and natural and mechanised ventilation and filtration.

* Corresponding author.
E-mail address: daniel.lester@rmit.edu.au (D. Lester).
[1] Mailing address: School of Engineering, RMIT University, Melbourne City Campus, VIC 3000, Australia.

http://dx.doi.org/10.1016/j.scitotenv.2021.152592

1. Introduction

Since the outbreak of the 2019 coronavirus disease (COVID-19) pandemic, indoor spaces have been the major venue for the disease to spread from person to person (Kenarkoohi et al., 2020; Noorimotlagh et al., 2021; Sodiq et al., 2021). COVID-19 is a respiratory disease caused by the severe acute respiratory syndrome coronavirus 2 (SARS-CoV-2). Spread of COVID-19 is affected by many factors including physical and socio-demographic factors (Gosak et al., 2021; Markovič et al., 2021). As the physical factors are concerned, although transmission of SARS-CoV-2 can occur via multiple routes, airborne transmission has been identified as the dominant route (Chirico et al., 2020; Greenhalgh et al., 2021; Zhang et al., 2020), hence quantification of airborne transmission risk is vital for risk management and mitigation in indoor environments.

Airborne transmission of SARS-CoV-2 involves three consecutive steps: (1) viral shedding via the emission of virus-laden respiratory droplets when an infected person is sneezing, coughing, speaking, and breathing; (2) transport and dispersion of the droplets in the air, during which the droplets dehydrate and become desiccated aerosol particles; and (3) inhalation of a sufficient dose of infectious particles by a susceptible person which initiates a new infection. The characteristics of each step can strongly affect the probability and outcome of infection. For example, the level of viral shedding is 20–30 fold higher with symptomatic COVID-19 patients than those without symptoms, and a "super spreader" can exhale 100 times more droplets than an average patient (Sehrawat and Rouse, 2021), significantly increasing the risk of infection. Furthermore, the expelled viral load can vary by over 1000-fold between different variants of SARS-CoV-2 (Li et al., 2021a), and significantly change over the infection period (Sender et al., 2021). The infectious dose (i.e., dose of virus needed to initiate an infection) also varies strongly between different SARS-CoV-2 variants (Liotti et al., 2021; Pollock et al., 2021; Sender et al., 2021), leading to vastly altered transmission dynamics. Conversely, wearing of facial masks or respirators by infected and/or susceptible people can greatly reduce the dose of virus emission and inhalation. Similarly, alteration of indoor ventilation airflows that transport virus-laden aerosols can have a profound impact on the transmission pattern. Ambient conditions such as air temperature and humidity also impact aerosol transport and evolution, specifically via droplet evaporation and vapor transport (Villermaux et al., 2017). All of the above factors need to be considered and quantified across the three transmission steps to effectively assess the risks associated with exposure to airborne SARS-CoV-2.

Due to the multidisciplinary nature of aerosol transport, there currently is some inconsistency regarding aerosol-related terminology across different disciplines (Tang et al., 2021). To avoid any ambiguity, this study uses the following definitions: (i) *Droplets* are defined as hydrated respiratory droplets that contain water and may be airborne or free falling. (ii) *Droplet nuclei* or *particles* are defined as dehydrated respiratory droplets that are airborne and water-free solid particles. (iii) *Aerosols* are defined as hydrated droplets or dehydrated droplet nuclei that are airborne.

Droplets emitted from human respiratory activities are distributed over a wide size range, typically from 100 nm to 1000 μm (Wölfel et al., 2020), as shown in Fig. 1 (hollow symbols and dashed curves). Given that a SARS-CoV-2 virus particle is ~100 nm in diameter (Bar-On et al., 2020), even submicron droplets can carry a few virions (a virion is a complete virus particle that consists of an RNA core and a protein coat and is the extracellular infectious form of SARS-CoV-2 (Yu et al., 2021)) and thus spread COVID-19. Although large droplets (>100 μm) contain more virions and so have a higher probability to trigger an infection if inhaled by a susceptible person, they can quickly deposit on to the ground or other surfaces (Yan et al., 2019b), and so do not play a major role in airborne transmission. Conversely, although small particles (<5 μm) contain fewer virions, these can remain

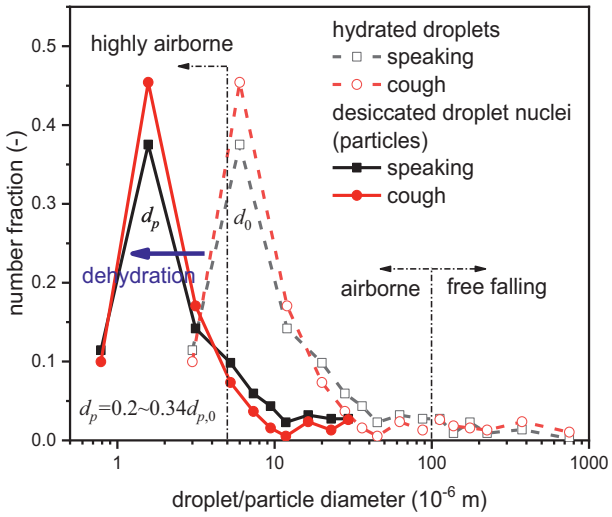

Fig. 1. Size distribution of human respiratory droplets (data from (Chao et al., 2009) and (Li et al., 2018)).

airborne for prolonged periods and thus cause "long-distance transmission" (Kwon et al., 2020). Sehrawat and Rouse (2021) argued that the most dangerous particle size is around 0.4 μm since these particles can access the lower lungs and alveoli, leading to increased infection risk and potentially damaging and lethal lesions. Sitting in between these "small" and "large" size regimes are medium-sized particles (5–100 μm) whose movement is jointly controlled by gravitational and inertial forces, and forces imposed by the background airflows (e.g., drag and lift forces, turbulent dispersion, etc.) (Yan et al., 2019b).

As expelled sputum droplets contain 95–99% water, they can dehydrate in the air and ultimately become desiccated droplet nuclei (or particles) which are 20–34% of the original hydrated size (Stadnytskyi et al., 2020), as illustrated by the solid symbols and curves in Fig. 1 (data from (Chao et al., 2009) and (Li et al., 2018)). Droplet evaporation in aerosol plumes is a highly complex process that is strongly affected by the ambient conditions, especially the local humidity and temperature surrounding the droplets and mixing of the vapor plume generated by the evaporating droplets (Villermaux et al., 2017). Thus the rate of evaporation of droplets can vary over several orders of magnitude in different indoor environments and depends strongly upon the fine-scale turbulent structure of the exhalation event (Chong et al., 2021; Villermaux et al., 2017). These processes mean that the evaporation and transport of droplets is highly variable, and particles which may otherwise be free-falling in one indoor space can become airborne for much longer periods in another. The challenge of airborne disease transmission modelling is to develop a framework that can account for these complex dynamics but is flexible enough to be readily applied to a wide range of practical indoor scenarios.

The Wells-Riley model (Riley et al., 1978) is widely used to estimate the transmission risk of airborne diseases, and has recently been extensively used (Li et al., 2021b; Liu et al., 2021; Zhang and Lin, 2021) for the evaluation of COVID-19 transmission. This model is based on the concept of a "quantum of infection" (Wells, 1955) under the assumption that the air in a given space is well-mixed and contains certain "quanta" of infectious pathogens (e.g., bacterium or virus). The probability of a susceptible person being infected accumulatively increases as they inhale more quanta over a period of exposure time. Although the Wells-Riley model is flexible and simple to use, this model is compromised as the quanta of infectious pathogens is often ill-defined for many viruses, and the assumption of well-mixed air conditions is often far from representative as sources of aerosolised pathogens are localised to infectious persons. Hence the classic Wells-Riley model does not

resolve the spatiotemporal inhomogeneity of the airborne pathogen distribution and thus infection risk, and the loosely defined infectious quanta cannot be clearly quantified from clinical data. Sze To and Chao (2010) suggested that in order to obtain effective risk assessments using the Wells-Riley model, the characteristics of a specific pathogen and the process of pathogen dispersion in a given indoor environment must be carefully addressed.

This study aims to address these shortcomings by developing a spatiotemporally resolved model of airborne COVID-19 transmission risk that addresses the above requirements. Clinical data of viral shedding by COVID-19 patients, and biomedical data regarding SARS-CoV-2 infecting human cells are formulated and incorporated into the basic Wells-Riley framework in Section 2, forming a novel, fit-for-purpose quantitative prediction model for airborne COVID-19 transmission risk. Computational fluid dynamics (CFD) simulations are used to predict the transport of droplet nuclei, providing accurate spatiotemporal distribution of virus-laden aerosol particles. These aerosol distributions serve as an input into the extended Wells-Riley model, forming an integrated model capable of predicting the spatially resolved infection risk associated with the exposure to SARS-CoV-2. In Section 3 this risk model is demonstrated via application to airborne COVID-19 transmission risk in a typical hospital ward. Spatially resolved infection risk maps are generated under a range of scenarios that include the impact of wearing respiratory PPE, and different variants of SARS-CoV-2 (including the highly contagious Delta variant). Conclusions are given in Section 4, including discussion of application of this model to a variety of scenarios.

The most significant contribution of this study is the development of a theoretical framework in which engineering designs and biomedical data can be incorporated to quantify epidemiological risks. To the best of our knowledge, the presented model is the first of its type and can be easily adapted for other airborne diseases. However, due to the lack of clinical and virological data regarding COVID-19 and SARS-CoV-2, some assumptions are not firmly validated by experimental evidence, such as the linear relationship between the HID_{50} and $TCID_{50}$ indices, and ignoring natural virus decay in the air. The model accuracy will increase when the relevant data become available.

2. A spatiotemporal model of COVID-19 transmission risk

2.1. The conventional Wells-Riley model

According to the original model proposed by Wells (1955) and Riley (Riley et al., 1978), the probability of infection via airborne particles is given by a Poisson process, where the infection probability P is dependent upon the total "infectious quanta" of pathogen inhaled $n_{quantum}$, which is given by the product of the number concentration of quanta in the air $c_{quantum}$, the susceptible person's pulmonary ventilation volumetric flow rate p, and the exposure time t_e as

$$P = 1 - \exp\left(-n_{quantum}\right) = 1 - \exp\left(-c_{quantum} p t_e\right) \tag{1}$$

Although not clearly defined by Wells and Riley, an infectious quantum is defined by Eq. (1), and so an infectious quantum represents a fixed number of virus particles (virions) that depends upon the infection rate of a single virion. Conventionally, the Wells-Riley model is used to determine airborne infection risk in ventilated indoor spaces under the assumption that the aerosol concentration (and hence $c_{quantum}$) is constant throughout. Consider a room with a ventilation rate Q. If the room contains I infected people, and each of them breathes out infectious pathogens at a fixed rate of q infectious quanta per person per unit time, then under equilibrium and well-mixed conditions the quantum concentration in the room is $c_{quantum} = Iq/Q$, and the infection probability of a person located in this room is

$$P = 1 - \exp\left(-\frac{Iqpt_e}{Q}\right). \tag{2}$$

This equation assumes that the infectious quanta are removed from the room air only by the ventilation airflow. In fact, however, many factors such as the accelerated decay of pathogens in air, ultraviolet deactivation, deposition of pathogen-laden particles, air purification, as well as chemical and thermal conditions will affect the pathogen viability and quantum concentration (Fisk et al., 2005). Over the past decades, a number of sink terms have been added to Eq. (2) to account for these factors (Sze To and Chao, 2010). Recently, Shen et al. (2021) has added scaling factors to account for the filtration effect of wearing personalised protective equipment (PPE) such as facial masks to mitigate against transmission of COVID-19. When all the above factors are considered, the updated Wells-Riley model takes the form

$$P = 1 - \exp\left(-(1-\eta_I)(1-\eta_S)\frac{Iqpt_e}{Q + \lambda_{decay}V + \lambda_{UV}V + \lambda_{dep}V + \ldots}\right), \tag{3}$$

where V is the room volume and λ_{decay}, λ_{UV} and λ_{dep} respectively represent the rate coefficients of quantum sinks due to natural pathogen decay, ultraviolet deactivation, deposition, etc. η_I and η_s are the filtration efficiency of the masks worn by the infected and susceptible persons, respectively.

One drawback of the zero-dimensional Wells-Riley model is the assumption of well-mixed and equilibrium conditions, corresponding to a homogeneous quantum concentration throughout the indoor airspace. This assumption is rarely satisfied due to the highly heterogeneous nature of indoor airflows and localised nature of infection sources such as individual patients. Hence the distribution of quantum concentration and infection risk typically exhibit strong spatial and temporal variations, which must be resolved to accurately quantify infection risk. With the increasing popularity of computational fluid dynamics (CFD) in modelling indoor air flow and contaminant transport in recent decades, the Wells-Riley model has been extended to 3D using CFD-generated aerosol concentration fields. Yan et al. (2017) developed a 3D predictive model to analyse airborne transmission risks in airliner cabins based on the Wells-Riley framework coupled with Lagrangian particle simulations. Srivastava et al. (2021) recently developed an analogous 3D model for COVID-19 infection evaluation in office buildings using Eulerian CFD simulations. In these studies the average concentration of infectious quanta $c_{quantum}$ in (1) is replaced by the spatiotemporal concentration $c_{quantum}(\mathbf{x},t)$, greatly improving the spatial resolution of the Wells-Riley model.

Another major drawback of the Wells-Riley model is that the infectious quantum has not been properly quantified. A properly quantified infectious quantum is important because different diseases have different transmissibility, therefore require different pathogen dose to initiate an infection (Sze To and Chao, 2010). Moreover, the dose of exposure also affects whether the outcome is subclinical, tissue damaging or even lethal following the infection (Sehrawat and Rouse, 2021). However, there currently is a severe lack of data regarding what represents an infectious quantum for a given disease or pathogen type. Although this problem has been pointed out by Sze To and Chao (2010) over a decade ago, there has been little progress in this field to date. Existing studies typically use hypothetical infectious quantum values, which severely limits the accuracy of risk predictions. This situation calls for accurate virological and clinical data to facilitate accurate quantification of the Wells-Riley model.

This paper will present a unified framework in which the infectious quantum is quantified using clinical data of viral shedding by COVID-19 patients and virological data of SARS-CoV-2 infecting human cells.

The local quantum concentration $c_{quantum}$ (Eq. (1)) in the air is characterised using temporospatial CFD simulations of aerosol transport considering a range of influencing factors including the HVAC scheme and wearing of PPE. This contributes to a fit-for-purpose predictive model for temporospatial infection risk of different SARS-CoV-2 variants in indoor spaces, and thus overcomes the limitations identified above.

2.2. Quantification of the infection risk of SARS-CoV-2

To properly quantify the infection risk of SARS-CoV-2 in the Wells-Riley model, it is necessary to link the number of infectious quanta $n_{quantum}$ to clinical data. Under the assumption that the number $n_{quantum}$ of infectious quanta inhaled scales linearly with the number n_{virion} of virions inhaled, then these variables may be related as

$$n_{quantum} = \xi n_{virion} \tag{4}$$

where the dimensionless coefficient ξ characterises transmissibility of the virus, which quantifies the average number of virions that need to be inhaled for infection to occur. From the Well-Riley model (1), this coefficient can be expressed in terms of the median human infectious dose HID_{50}, which is defined as the dose of virus needed to infect 50% of the population, hence

$$P = 0.5 = 1 - \exp(-\xi HID_{50}) \tag{5}$$

and so ξ is related to HID_{50} as

$$\xi = \frac{\ln 2}{HID_{50}} \tag{6}$$

Although HID_{50} data for SARS-CoV-2 is currently limited, transmissibility data is available in terms of the median tissue culture infectious dose $TCID_{50}$, which is defined as the dose of virus needed to infect 50% of the tissue cultures in laboratory (van Doremalen et al., 2020). A smaller $TCID_{50}$ value means less virions are needed to initiate an infection and hence a more contagious virus. For example, the $TCID_{50}$ unit of human immunodeficiency virus (HIV) is about 116,000 virions (Iwami et al., 2012), while for influenza A virus the unit is 1000 to 6000 virions with a mean value of 4000 (Parker et al., 2015; Yan et al., 2019a). $TCID_{50}$ data for SARS-CoV-2 has only recently been reported, with variation over a very wide range (between 10^3 and 10^5 virions) depending on the virus variant (Liotti et al., 2021; Pollock et al., 2021; Sender et al., 2021). It is expected that as further studies are conducted that these data shall become more robust, but similar to viral load, large variations in transmissibility may persist between SARS-CoV-2 variants. Under the assumption that there exists a linear relationship between the in-vitro $TCID_{50}$ index and the in-vivo HID_{50} index, Eq. (6) may be expressed as

$$\xi = \frac{\ln 2}{\delta TCID_{50}}, \tag{7}$$

where the coefficient δ represents the ratio of HID_{50} to $TCID_{50}$ ($\delta = HID_{50}/TCID_{50}$). For influenza, the HID_{50} unit is reported to be 1 to 126 $TCID_{50}$ units with the median value of $\delta = 5$ (Nikitin et al., 2014) and $\delta = 0.5$ to 3 for those not immunised. For SARS-CoV-2, δ is unknown but we currently assume it to be the same as that of the influenza virus ($\delta = 5$) in lieu of more detailed information.

In the initial stage of the COVID-19 pandemic, Wölfel et al. (2020) continuously monitored the SARS-CoV-2 viral load in the sputum of COVID-19 patients and found that viral shedding was very high during the first week of symptoms, followed by a slowly descending viral load in the following 3 weeks. Over a 28-day period, the mean viral load in the patients' sputum was 7.0×10^6 ribonucleic acid (RNA) copies/mL, with a maximum of 2.35×10^9 copies/mL. The number of virions has been found (Sender et al., 2021) to be roughly equal to the number of RNA copies. Assuming each genome is associated with a virion, Stadnytskyi et al. (2020) calculated that the probability that a 50-μm hydrated droplet contains at least one infectious virion is ~37%. For a 10-μm and 3.5-μm hydrated droplet, the probability drops to 0.37% and 0.01%, respectively. This suggests a linear relationship between the virion count in a respiratory droplet and the volume of the droplet, which can be expressed as

$$n_{p,virion} = c_{RNA}\frac{\pi d_{p,0}^3}{6}, \tag{8}$$

where $n_{p,virion}$ is the number of virions contained in a droplet with an initial hydrated diameter of $d_{p,0}$ and c_{RNA} is the viral load of an infected person's respiratory fluid (RNA copies per unit volume).

As a droplet evaporates and ultimately becomes a desiccated particle, it shrinks to a diameter of d_p although the number of virions contained in it does not change. Therefore, for air with a local particle volume fraction of $c(\mathbf{x},t)$, the local number concentration of virions is

$$c_{N,virion}(x,t) = \frac{c(x,t)d_{p,0}^3}{d_p^3}c_{RNA}, \tag{9}$$

and so the local number concentration of infectious quanta is

$$c_{quantum}(x,t) = \xi c_{N,virion}(x,t) = \xi\frac{c(x,t)d_{p,0}^3}{d_p^3}c_{RNA}, \tag{10}$$

Substitution into Eq. (1) yields a spatiotemporal Wells-Riley model for the local infection risk of SARS-CoV-2 based upon the local particle concentration.

$$P(x,t) = 1 - \exp\left(-(1-\eta_S)\frac{\ln 2}{\delta TCID_{50}}\frac{c(x,t)d_{p,0}^3}{d_p^3}c_{RNA}pt_e\right), \tag{11}$$

where the coefficient η_S ($0 < \eta_S < 1$) is the filtration efficiency of respiratory PPE worn by susceptible persons. Conversely, respiratory PPE worn by infected person reduces the load of expelled aerosols and so is accounted for during the modelling of particle release and transport using CFD, and ultimately impacts $c(\boldsymbol{x}, t)$. CFD can accurately simulate physical aerosol transport and thus directly account for the quantum sink terms in Eq. (3) associated with particle deposition and filtration in a physically consistent manner. Similarly, if significant, impacts such as particle decay and UV degradation can incorporated into the CFD simulations via appropriate models.

However, changes in the viability of the suspended virions with the aerosols are not considered in this study due to the very strong viability of SARS-CoV-2 in the environment. van Doremalen et al. (2020) studied the viability of the virus in aerosols, and found that the virus remained highly viable throughout the duration of their experiment (3 h), with a reduction in the infectious titre from $10^{3.5}$ to $10^{2.7}$ $TCID_{50}$ per litre of air, equivalent to a half-life of 1.1 to 1.2 h, compared to the typical particle residence time of 5–15 min in a well-ventilated room with an air exchange rate of 12 air changes per hour (ACH) (Tang et al., 2021). Therefore, the rate of degradation is regarded as very small and may be negligible under normal mandated air exchange rates. In addition, due to the lack of clinical and virological data regarding COVID-19 and SARS-CoV-2, some assumptions are not firmly validated by experimental evidence, such as the linear relationship between the HID_{50} and $TCID_{50}$ indices, and ignoring natural virus decay in the air. The model accuracy will increase when the relevant data become available.

It is important also to note that the modified Wells-Riley model (11) assumes that the infection risk only depends upon the total

viral load inhaled (given by the total volume of inhaled aerosols) and does not depend upon the particle size distribution of inhaled aerosols. Several studies have shown (Inthavong et al., 2013) that the size of inhaled aerosols governs the deposition of such aerosols in lungs and upper airway, with smaller particles penetrating the lower airway and alveoli, causing an elevated risk of infection. A particle size-dependent transmission coefficient ξ is required to properly incorporate these effects into the Wells-Riley model, but such clinical data is not yet available and so this issue is beyond the scope of this study.

2.3. Spatiotemporal resolution of aerosol transport

Eq. (11) suggests a key to spatiotemporal resolution of COVID-19 infection risk is to properly characterise the concentration distribution of virus-laden airborne particles. For engineering-level applications, multiphase flow models based on the Reynolds-averaged Navier-Stokes (RANS) equations are often used to predict the transport of airborne particles. High fidelity methods such as Large Eddy Simulation (LES) and Direct Numerical Simulation (DNS) are useful for scientific studies but are typically too computationally expensive for widespread application. RANS models solve conservation equations and turbulence models for the air flow field. There exist two classes of methods used to describe the transport of particles, termed Lagrangian and Eulerian methods, which have characteristic advantages and disadvantages.

The Lagrangian method addresses the disperse nature of the aerosol phase and tracks the movement of individual particles via Newton's second law. The Lagrangian method determines the lift, drag, gravitational and Basset forces on an ensemble of representative aerosol particles of a given initial size distribution (under the assumption of negligible aerodynamic interactions between aerosols), and so resolves spatiotemporal evolution of the aerosol particle size distribution. The Lagrangian method can also account for various interphase transport phenomena such as interfacial forces and droplet evaporation. It is widely used in the studies of indoor particulate contaminants (Yan et al., 2017) including the transmission of COVID-19 (Li et al., 2021b; Liu et al., 2021). However, additional post-processing procedures (such as smoothing kernels) must be implemented to convert the discrete particle trajectories to a continuous particle concentration field (Yan et al., 2017; Zhang and Chen, 2007) before the risk model can be applied, and large particle numbers must be advected to provide sufficient resolution to avoid conversion errors (Evrard et al., 2021).

In contrast, the Eulerian models treat the particulate phase as a continuous pseudo-fluid that interpenetrates the air, thus their transport can be modelled using a set of coupled conservation equations, with the particle concentration directly calculated. Depending on how the conservation equations are solved for the particulate phase, the Eulerian models have different variants, such as the two-fluid model, algebraic slip model (ASM), multiple size group (MUSIG), and many others. The two-fluid model solves two sets of conservation equations, one for each phase, with interphase transport terms being included in the conservation equations to account for the interphase transport processes. The algebraic slip model treats the air-particle mixture as a single-phase fluid, thus only solves one set of momentum conservation equations for the mixture and a further scalar conservation equation for the particulate phase volume fraction. Momentum transfer between phases is encoded via an algebraic "slip velocity" within the particulate phase volume fraction conservation equation. In comparison, the two-fluid model can produce more physically robust predictions but is computationally more expensive than the algebraic slip model. The two-fluid and algebraic slip models are somewhat limited in that they can only model a single representative particle size (encoded in the momentum transfer terms), and so cannot resolve evolution of the particle size distribution. MUlti-SIze-Group (MUSIG) models (Li et al., 2010; Yuan et al., 2016) overcome this restriction by using a series of momentum equations for various particle size "bins" (with different momentum exchange terms for each) to resolve the evolving particle size distribution, but the resultant large equation system is computationally expensive to solve. The governing equations and related closure equations of the above models have been extensively elaborated in the literature (Li et al., 2015; Mikko et al., 1996) and will not be repeated here. In principle, the spatiotemporal Wells-Riley model (11) can be used with any appropriate CFD method for a given application. However, to provide some guidance as to method selection, we evaluate the Lagrangian (LM), two-fluid (TFM) and algebraic slip (ASM) models in terms of accuracy and computational cost to simulate the transport of micron-sized particles in a ventilated chamber against experimental data measured via phase Doppler anemometry (PDA) (Chen et al., 2006). Details regarding the model setup and numerical procedure can be found in (Li et al., 2015), and only data comparison are shown here for conciseness.

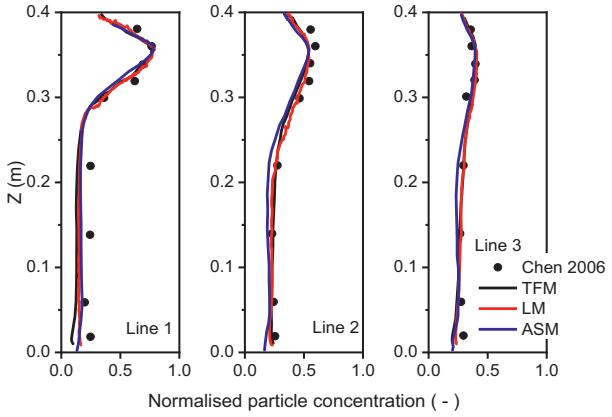

Fig. 2. Comparison of two-phase flow models against experimental data.

Fig. 2 compares the particle concentration distribution predicted from CFD simulations against the experimental measurements. It shows that all the three two-phase flow models achieve good agreement with an average predictive error smaller than 5%. The computational time for each model on a desktop computer with a 4-core CPU (3.3 GHz base speed) and 16 GB RAM is shown in Table 1. It shows that the algebraic slip model (ASM) only needs 180 min to obtain the particle concentration field, whereas the two fluid model (TFM) requires 300 min due to solution of the two momentum phase equations. The Lagrangian model (LM) needs a considerably longer compute time (540 min) due to the need to solve the particle advection equations, and the subsequent post-processing to convert the discrete particle locations into a continuous particle concentration distribution.

Despite the clear advantages in computational overhead, it is still worth reiterating that the algebraic slip model is relatively simplified, while the two-fluid and Lagrangian models provide more physically robust approaches to particle transport in the air by accounting for phenomena such as lift, Magnus and Basset forces. In addition, these models also allow for dynamic models of droplet evaporation. Furthermore, the algebraic slip model and two-fluid model should only be used when the aerosol plume can be validly represented by a single particle size, i.e. when evolution of the particle size distribution is negligible. Thus, it is important to select appropriate multiphase

Table 1
Compute time of CFD methods.

Time (min)	TFM	LM	ASM
Model solution	300	360	180
Post-processing	0	300	0
Total	300	540	180

flow models and associated closures for the physical scenario at hand and the simulation fidelity demanded by the application.

3. Application of COVID-19 infection risk model in a hospital ward

As a demonstration, the spatiotemporal Wells-Riley model (11) developed in Section 2 is applied to the case of airborne COVID-19 infection risk in a hospital ward. We consider the impact upon airborne infection risk of COVID-19 variant, virus transmissivity, and whether respiratory PPE is donned by patients and/or staff. Quantification of airborne infection risk using a realistic floor plan and HVAC settings will provide important information to develop effective mitigation and protection strategies.

3.1. The hospital ward model

Shown in Fig. 3 is the hospital ward of consideration, which includes 4 patient rooms, a nursing station and a workroom. The total floor area of the section is 162 m^2 and the floor aera of each patient room is 13.6 m^2. Human models (downloaded from https://grabcad.com/mcramblet-1/models) are included in the ward model to account for the metabolic heat generated by human bodies. The ward has a mixing ventilation scheme where both the supply and exhaust vents are located in the ceiling. To balance the pressure inside and outside the patient rooms when the room doors are closed, bent pipes with inserted high-efficiency particulate air (HEPA) filters are used to connect the rooms and corridor. However, due to the flow resistance of the filters, a significant part of air leaks through the door gaps into the work area, and so can be a major source of infection in the work area (Villafruela et al., 2016).

To reduce the computational overhead of the model, two separate computational domains were created, one for Patient Room 3 and the other for the common ward area, rather than computing the whole ward section, as shown in Fig. 4. It is assumed that the aerosol concentrations in the leaked air from each room are equal as they are all single-bed rooms containing one infected person. This allows us to only simulate one patient room, and hence reduce the CPU time. The patient room model will be used to analyse the transport characteristics of aerosol particles so that the particle size can be properly characterised and their transport characteristics can be actually predicted. The room model will also generate important data to properly specify boundary conditions of the work area model.

The computational domains shown in Fig. 4 were discretised using an unstructured tetrahedral mesh with prism inflation layers applied at all solid surfaces for improved modelling of near-wall flows, heat transfer and aerosol deposition. Mesh independence is achieved at 2.2 million and 10.8 million mesh elements for the patient room and work area models, respectively, as further increasing the mesh count to 2.8 and 12.2 million elements respectively results in <0.5% change in the predicted air velocity at randomly selected locations.

The ventilation and heat load parameters of the ward, as well as the respiration and aerosol emission data of the occupants (e.g., healthcare worker and patients) are summarised in Table 2. The ventilation parameters are selected based on the ASHRAE Standard 55-2004 (ANSI, 2004). The total human metabolic heat is ~90 W/person, of which around 40% (36 W) is dissipated through convection in a typical indoor environment (de Dear et al., 1997). This study only considers the convective component as other components (e.g., radiative, sweating, etc.) are not expected to remarkably affect the airflow field and aerosol transport. The average human pulmonary ventilation rate is 6 L/min (Carroll, 2007), which corresponds to a total mass flux of exhaled aerosol particles by a patient is 2.0×10^{-10} kg/s, as calculated in Section 3.2.

3.2. Aerosol transport modelling approach

As discussed in Section 1, the particle size strongly affects the transport characteristics of aerosol particles, therefore proper characterization of the particle size is critical to effective modelling. Previous studies (Li et al., 2018) have demonstrated that isolated droplets as large as 100 μm only need 5 s to become completely desiccated in typical indoor conditions (25 °C, 50% relative humidity), however this evaporation time can be extended significantly in the presence of high

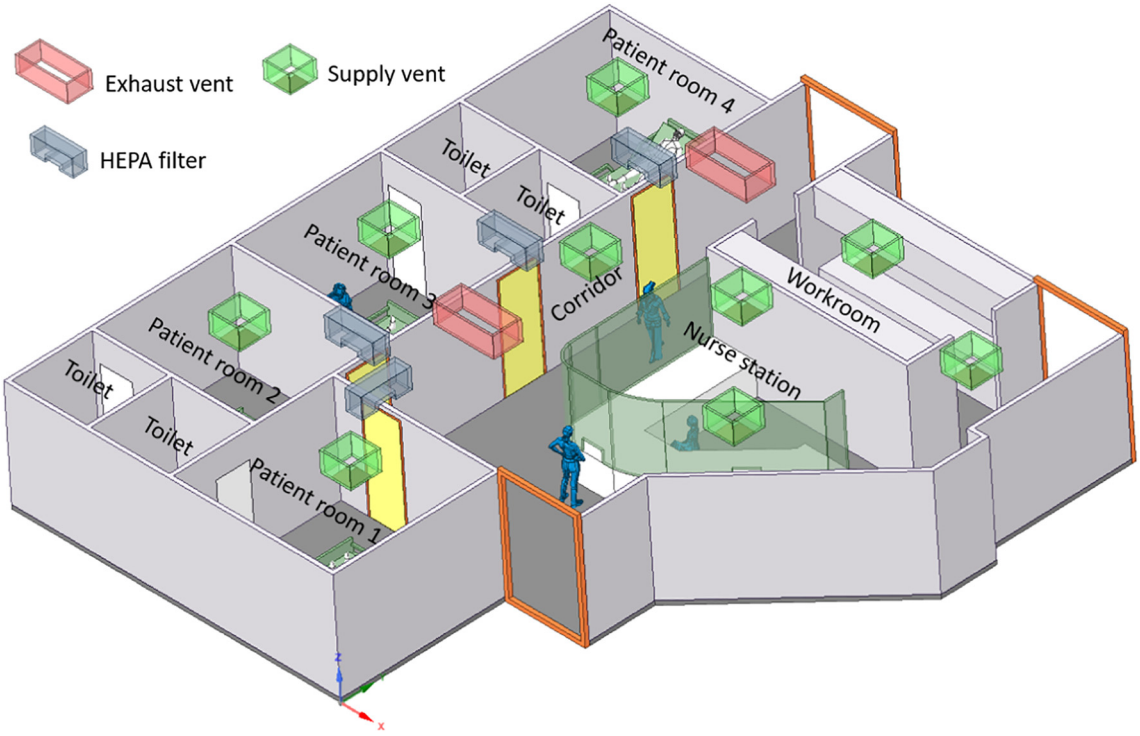

Fig. 3. CAD model of the hospital ward (the ward includes 4 single-bed patient rooms, a nurse station and workroom).

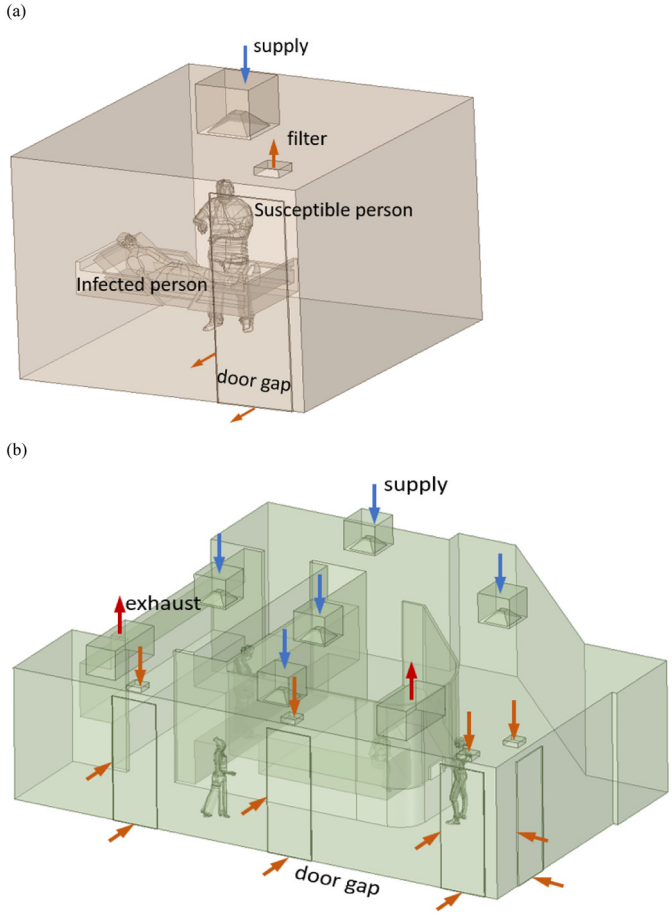

Fig. 4. The computational domains for (a) patient room 3 and (b) the main ward area (the orange arrows point to the gaps in the door leading to air leakage, all other flow enters or leaves the room through the supply air (blue arrow) and return air (red arrow)).

humidity or for dense sprays where the surrounding vapor field significantly retards evaporation (Chong et al., 2021; Villermaux et al., 2017). Under the above fast-evaporation conditions, this evaporation time reduces to 0.1 s for droplets with initial size of 10 μm. As a result, over 80% of the respiratory droplets will be desiccated and thus become airborne droplet nuclei (<10 μm) within 1.0 s and more than 95% of the droplets will shrink to be less than 30 μm in few seconds. In comparison, the particle residence time in a well-ventilated hospital room with an air exchange rate of 12 air changes per hour (ACH) is 5–15 min (Tang et al., 2021), rending the droplet dehydration time negligible. Therefore, this study neglects the process of droplet dehydration, and assumes that droplets become desiccated particles immediately after being emitted. As the density and load of non-volatile compounds in human sputum respectively is 1400 kg/m^3 and 1.8% (Nicas et al., 2005), the diameter d_p of a dehydrated droplet nucleus is estimated to be 26.2% of its original diameter $d_{p,0}$. As a result, more than 95% of the particles will be smaller than 30 μm according to Fig. 1.

Table 2
Computational parameters of the hospital ward models.

Building		Occupants		
ACH	Supply air temperature	Convective heat	Aerosol emission rate	Pulmonary ventilation rate
(−)	(°C)	(W/person)	(kg/s/patient)	(L/min/person)
12	21	36	2.0×10^{-10}	6

To understand the transport characteristics of different-sized particles, CFD simulations using the Lagrangian model are first performed with the ejected particle size distribution given in Fig. 1 for human speaking. The trajectories of particles with different sizes are shown in Fig. 5. The results show that as the particles disperse, the tendency to deposit increases with particle size, such that 1.6-μm particles follow the air flow and remain airborne with minimal deposition (Fig. 5(a)), but 11.8-μm particles are found to deposit on the floor and room walls (Fig. 5(b)). Deposition becomes dominant for 22.9-μm and 29.5-μm particles (Fig. 5(c) and (d)), where most of these sized particles settle in a small area around the patient mouth, and some of the 22.9-μm particles settle on the floor. As a result, almost all particles larger than 20 μm settle in the room and cannot pass through the door gaps and enter the work area. These results demonstrate it is typically safe to ignore particles larger than 20 μm in terms of airborne disease transmission risk, and so these particles shall not be considered further in this study.

According to Fig. 1, although particles larger than 20 μm comprise a large mass fraction (>80%) of the exhaled aerosol, they only comprise a small number faction (<5%). The number and mass fractions distribution of particles smaller than 20 μm are shown in Fig. 6.

The algebraic slip model is selected to predict the aerosol transport due to its good accuracy and relatively low computational cost. However, due to the inherent limit of the model, a representative particle size rather than the particle size distribution as shown in Fig. 6 must be used. Therefore, the size and mass distributions shown in Fig. 6 are then used to calculate a representative volume-weighted mean particle diameter ($d_{p,mean}$). If the particle size range is binned into i size groups and each group contains j_i particles, the volume-weighted mean particle diameter $d_{p,mean}$ then satisfies

$$d_{p,mean}^3 \sum_i j_i = \sum_i \left(d_{p,i}^3 j_i \right), \tag{12}$$

resulting in $d_{p,mean} = 6.62$ μm. The volume-weighted mean particle diameter $d_{p,mean}$ is incorporated in the algebraic model to predict the transport of particles in the air. The predicted particle distribution and deposition pattern are compared with those generated from the Lagrangian model using the particle size distribution shown in Fig. 6. As shown in Fig. 7, both models predict a highly heterogeneous particle concentration field in the room, with a local high concentration region directly above the patient's head. The particles quickly disperse as the distance from the patient increases. The ASM with the representative particle mean diameter $d_{p,mean}$ predicts a very similar spatial aerosol distribution to that of the Lagrangian model. Similarly, the particle deposition patterns predicted from both models are also very similar, resulting in a net particle deposition rate at the floor of 5.1×10^{-12} and 6.2×10^{-12} kg/s, for the algebraic slip model and Lagrangian model respectively. Although these comparisons do not extensively test evolution of the particle size distribution, these results indicate the algebraic slip model is sufficiently accurate for demonstration of the spatiotemporal Wells-Riley model.

3.3. Effects of virus features on the infection risk

As discussed in Section 2, infection risk depends on a range of factors. Understanding the importance of each factor is important to the development of effective prevention and protection strategies. To quantify the effects of virus characteristics (e.g., the $TCID_{50}$ unit and viral load) on the infection risk, computations are performed under a variety of assumed scenarios. In the computations of Fig. 8, the susceptible person wears a surgical mask with a filtration efficiency of $\eta_S = 0.715$ (Clapp et al., 2021), the infected person wears no mask ($\eta_I = 0$), and the particle emission rate is 1000 particles per second (Stadnytskyi et al., 2020), equivalent to a mass injection rate of 2.0×10^{-10} kg/s.

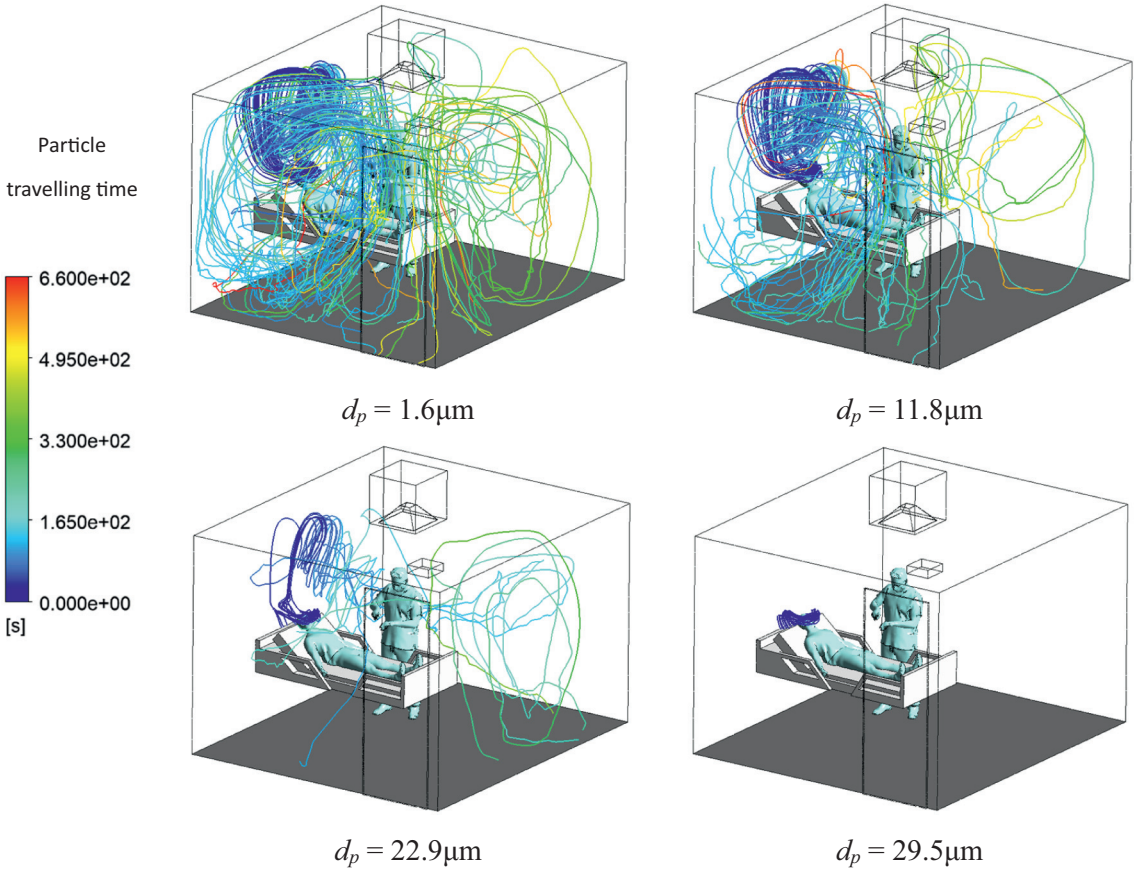

Fig. 5. Trajectories of different sized aerosol particles computed from a single exhalation event under the Lagrangian model.

We first investigate the sensitivity of infection risk to the number of virions needed to initiate an infection, given in terms of the $TCID_{50}$ value. Different viruses can have markedly different $TCID_{50}$ values, which is one of the most important factors determining the viruses' transmissibility. For SARS-CoV-2, the $TCID_{50}$ unit is reported to range from 10^3 and 10^5 virions with an average value of 10^4 virions (Liotti et al., 2021; Pollock et al., 2021; Sender et al., 2021). For the original SARS-CoV-2 variants such as Alpha and Beta, the $TCID_{50}$ unit is around 10,000 (Sender et al., 2021). The Delta variant possesses mutated spike proteins that have a stronger ability to bind to human cells (Ma et al., 2021). The study by Scudellari (2021) found that in the Alpha variant of SARS-CoV-2, around 50% of spike proteins are primed to infect a human cell. This percentage rises to greater than 75% in the Delta variant, making it need fewer virions to start an infection (i.e., a smaller $TCID_{50}$ unit) compared to non-Delta variants. As a result, $TCID_{50}$ unit of the Delta variant is around 4000 (Liotti et al., 2021).

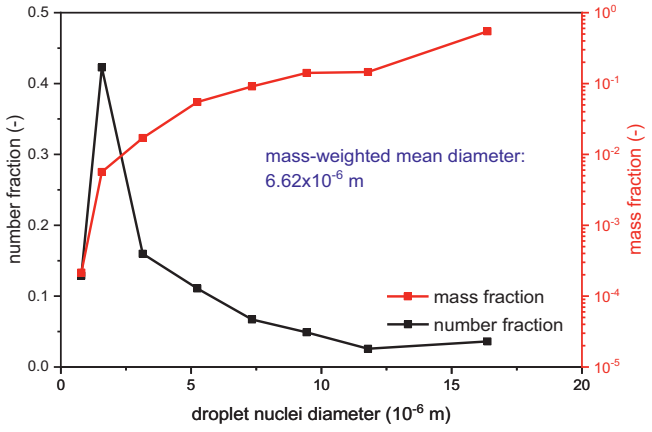

Fig. 6. Number and mass fraction probability distributions of dehydrated aerosol particles.

Infection risk in the patient room is quantified in terms of the 3D distribution of infection probability given by (11) using an assumed total exposure time of 1 h (t_e = 3600 s) and a viral load of C_{RNA} = 2.35 × 10^9 copies/mL (the peak value of the original variants measured by Wölfel et al. (2020)). As shown in Fig. 8, the computations reveal that the infection risk has a strongly heterogeneous distribution similar to that of the particle concentration field (Fig. 7(b)). As expected, the region above the infected person represents the highest infection risk. The infection risk is relatively low when the $TCID_{50}$ unit is large (1 × 10^5 virions) even the infected person does not wear a mask and the susceptible person only wears a surgical mask with a filtration efficiency of 0.715. The area-averaged mean infection probability in the horizontal plane at the typical nose height of the susceptible person (H = 1.65 m) is as low as 0.028. As the $TCID_{50}$ unit decreases and the viruses become more contagious, the infection risk quickly increases. When the $TCID_{50}$ unit drops to 1 × 10^3, the mean infection probability at the nose height becomes more than 16 times higher than that of $TCID_{50}$ = 1 × 10^5.

Apart from the $TCID_{50}$ unit, the viral load c_{RNA} is another critical parameter determining the transmissibility. The viral load reported in the literature is distributed in a very wide range (10^2 to 10^{11} RNA copies/mL (Miller et al., 2021)) and can vary with different virus variants. Li et al. (2021a) reported that the viral load produced by the Delta variant is over 1000 times higher than the original 19A/19B strain, and this variation is one of the main causes of the Delta variant's high transmissibility. To investigate

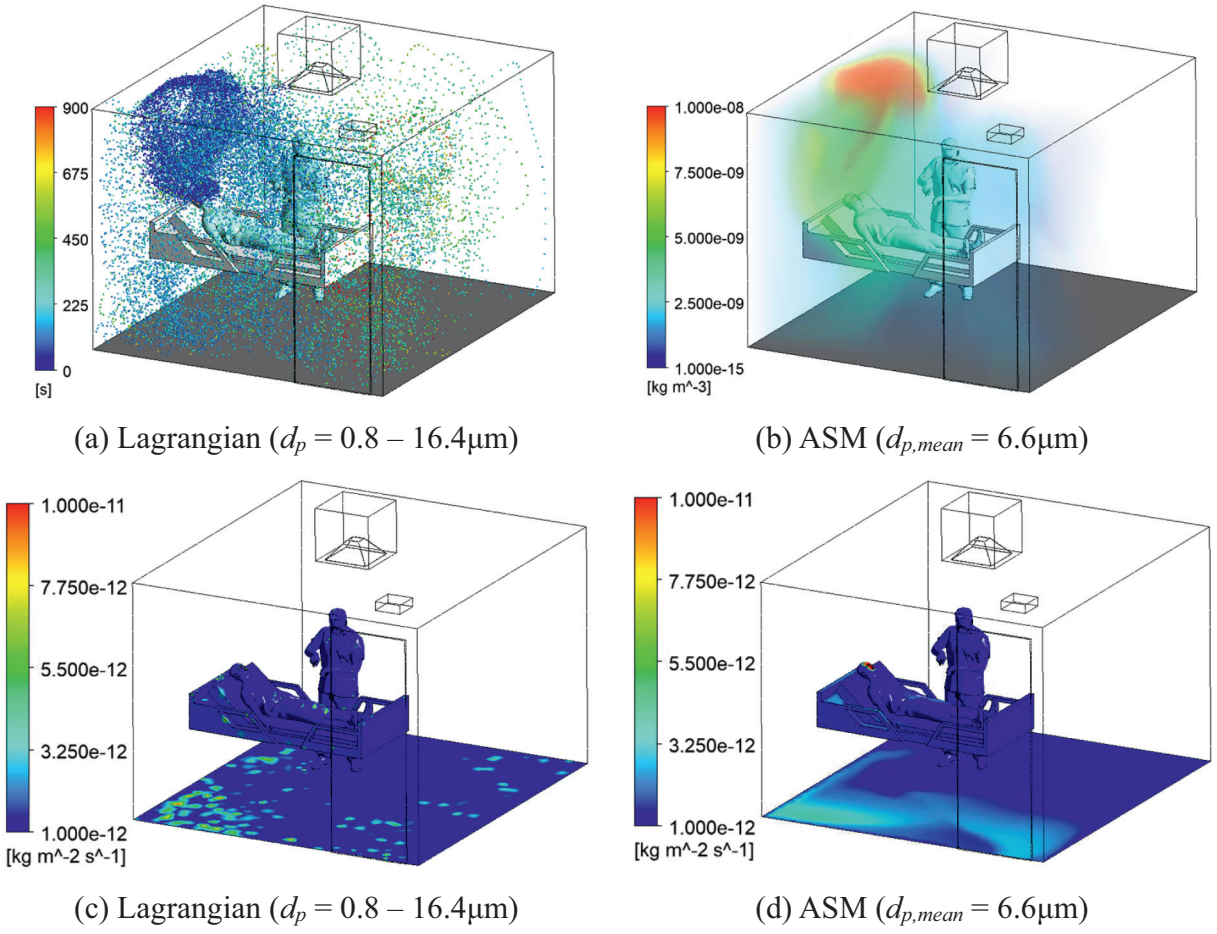

Fig. 7. Comparison of (a), (b) particles in the air and (c), (d) particle deposition pattern for the Lagrangian and algebraic slip models respectively. Note that (a) shows the particle traveling time and (b) shows the particle concentration field. (c) and (d) show the particle deposition rate. The figure shows a properly selected representative particle size is able to achieve a satisfactory prediction.

the effects of viral load on the infection risk, computations are performed over the range of 6×10^5 to 1×10^{11} copies/mL. The lower limit of viral load (6×10^5 copies/mL) represents the minimum viral load to trigger an infection in vitro (Li et al., 2021a) and the upper limit (1×10^{11} copies/mL) is the maximum value reported in the literature (Miller et al., 2021). Fig. 9 shows the infection risk pattern in the room under different viral loads. The infection probability is very low at low viral loads (Fig. 9(a) and (b)), but gradually increases as the viral load becomes larger and begin to display heterogeneous distribution patterns (Fig. 9(c)). At very high viral load (1×10^{11} RNA copies/mL), a significant part of the room becomes a "red zone" (Fig. 9(d)) with a mean infection probability of 0.767 for a one-hour exposure.

To comprehensively analyse the relative significance of the $TCID_{50}$ unit and viral load, parametric studies are performed. The computations are completed with an exposure time of 1.0 h (t_e = 3600 s) and the susceptible person wears a surgical mask (η_S = 0.715 (Clapp et al., 2021)). The predicted mean infection risk at the nose height is shown in Fig. 10, which indicates that the infection risk is very low at small viral loads ($c_{RNA} < 10^7$ copies/mL), but increases nonlinearly as the viral load becomes larger. This results in an apparent "threshold viral load", beyond which the infection risk rapidly increases, and this threshold viral load increases with $TCID_{50}$ value.

The parametric studies show either a large viral load or small $TCID_{50}$ unit can lead to a high infection risk. Highly contagious variants of SARS-CoV-2 such as Delta are typically characterised by high viral loads and small $TCID_{50}$ values, rending them much more contagious than the original variants.

Using a $TCID_{50}$ unit of 4000 virions for the Delta variant (Liotti et al., 2021) and 10,000 virions for the original variants (Sender et al., 2021), the corresponding infection risks of the variants are estimated and plotted in Fig. 10. With the same aerosol concentration, the infection risk of the Delta variant is significantly higher than the original variants. Moreover, given that the viral load produced by the Delta strain is 3 orders of magnitude larger than the original SARS-CoV-2 variants (Li et al., 2021a), the mean and maximum viral load produced by the Delta variant is estimated to be 8.82×10^9 and 2.96×10^{12} copies/mL respectively based on the study of Wölfel et al. (2020). Consequently, the average infection probability of the Delta variant is estimated to be more than 200 times greater than the original variants, as illustrated by the red dots in Fig. 10. If we consider the maximum viral load, the transmissibility of the Delta variant is even more striking. Newly emerged variants such as the C.1.2 (Scheepers et al., 2021) and the B.1.1529 strains are reported to have highly mutated spike proteins, which could lead to dramatically increased infection risk.

If the susceptible person wears a surgical mask (η_s = 0.715), this can provide good protection from the original SARS-CoV-2 variants, but the protection is limited in the case of the Delta variant, which means that more effective protection strategies need to be developed urgently.

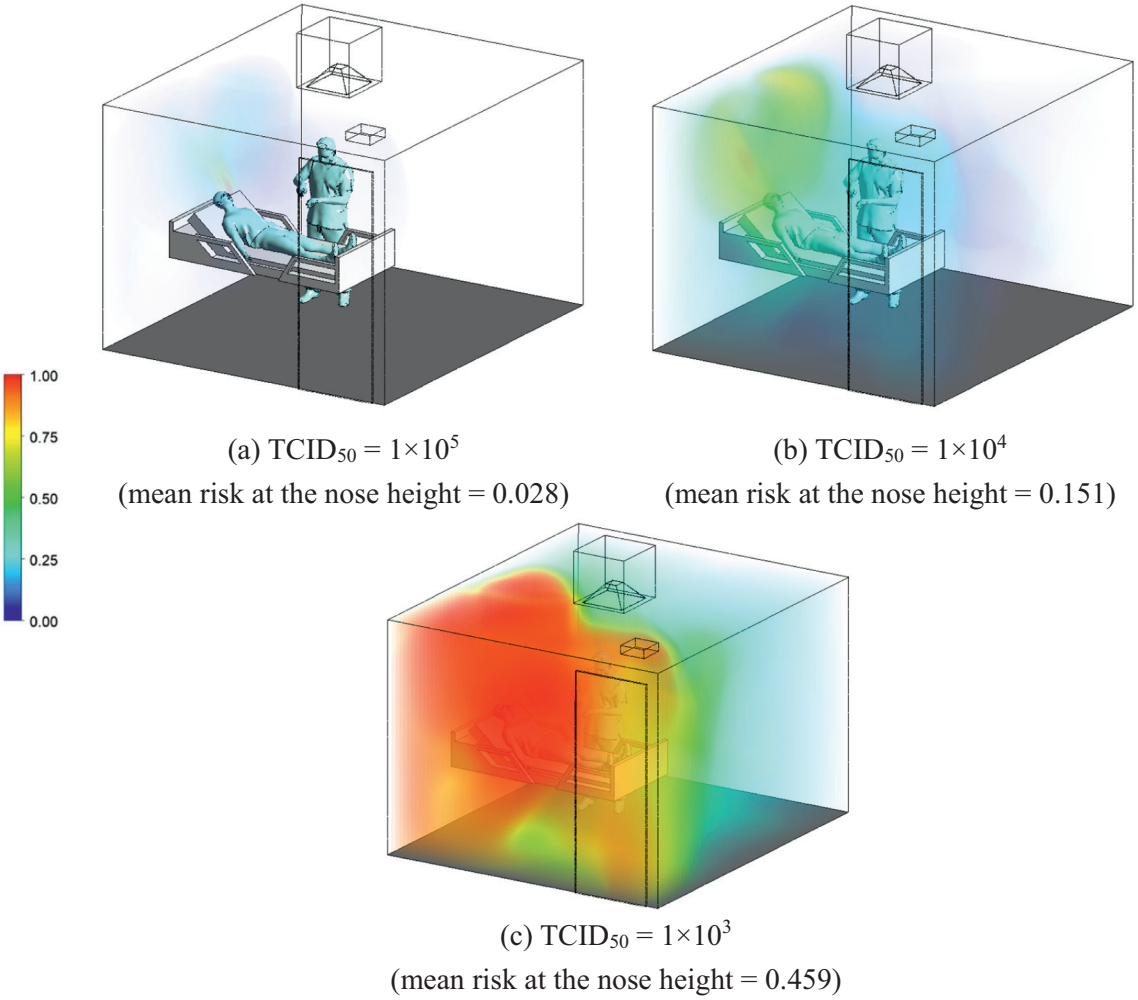

Fig. 8. Effects of the $TCID_{50}$ on the infection risk ($\eta_I = 0$, $\eta_S = 0.715$, $c_{RNA} = 2.35 \times 10^9$ copies/mL, $HID_{50} = 5 \times TCID_{50}$, $t_e = 3600$ s. Nose height taken as H = 1.65 m). The results show when other conditions remain unchanged, the infection risk quickly increases as the $TCID_{50}$ unit decreases.

3.4. Effects of personal protection equipment (PPE) on the infection risk

The use of respiratory personal protective equipment (PPE) by both the infected and susceptible persons is also investigated. Computations were completed with the infected person wearing either no mask ($\eta_I = 0$) or a mask with a filtration efficiency of 0.9 ($\eta_I = 0.9$). This means the net particle injection rate from each infected person into the air reduces from 2.0×10^{-10} kg/s to 2.0×10^{-11} kg/s. Surgical masks and NIOSH-approved N95 respirators are selected for the susceptible person, with respective filtration efficiencies of $\eta_s = 0.715$ and $\eta_s = 0.98$ (Clapp et al., 2021). Other computational parameters are selected for the Delta variant ($c_{RNA} = 8.82 \times 10^9$ copies/mL, $TCID_{50} = 4000$), an exposure time of $t_e = 3600$ s is used, and the predicted infection risk distribution is shown in Fig. 11.

As expected, the results indicate that wearing of facial masks by the infected and/or susceptible persons markedly reduces the infection risk. As shown in Fig. 11(a), when the infected person is not wearing a mask and the susceptible person only wears a surgical mask, the room has a local infection risk approaching 1.0 over a one-hour exposure. The mean infection probability at the nose height is 0.415. However, if the susceptible person wears a N95 respirator, the risk drops significantly to 0.118 (Fig. 11(b)). It is also important for the infected person to wear a facial mask in order to reduce aerosol emission and hence source of infection. When 90% of the emitted particles are captured by the mask, the mean infection probability drops from 0.415 (Fig. 11(a)) to 0.152 even if the susceptible person only wears an ordinary surgical mask (Fig. 11(c)). The mean risk further drops to 0.017 if the susceptible person wears a properly fitted N95 respirator (Fig. 11(d)). The results clearly demonstrate the efficacy of respiratory PPE for both patients and healthcare workers in healthcare environments.

Parametric studies are also conducted to analyse the effectiveness of respiratory PPE over a broad parametric range, as shown in Fig. 12. Fig. 12(a)–(c) presents the results of cases where the infected person is not wearing a mask and in Fig. 12(d)–(f), the infected person wears a mask with a filtration efficiency of 0.9. In each column of the figures, the viral load increases from 1×10^7 copies/mL in the top to 1×10^{11} copies/mL in the bottom. The results clearly show that wearing a mask or respirator by the infected and/or susceptible persons can contribute to lower infection risks, and the benefits increase with mask filtration efficiency.

However, the efficacy of respiratory PPE can dramatically change under different viral load and $TCID_{50}$ conditions. For example, when the viral load is low ($c_{RNA} = 10^7$ copies/mL), wearing a N95 mask ($\eta_S = 0.98$) by the susceptible person can keep the infection risk at very low levels (<0.001) even if the infected person wears no mask and the virus is highly contagious ($TCID_{50} = 10^3$), as shown in Fig. 12 (a). If the infected person can also wear a mask, it is safe for the susceptible person to only wear a surgical mask Fig. 12(d). However, with increasing viral load in the particles, the effectiveness of respiratory PPE quickly decreases. If we take the infection probability of 0.001 as the acceptable upper limit (illustrated by the blue dash-dot lines in the figure),

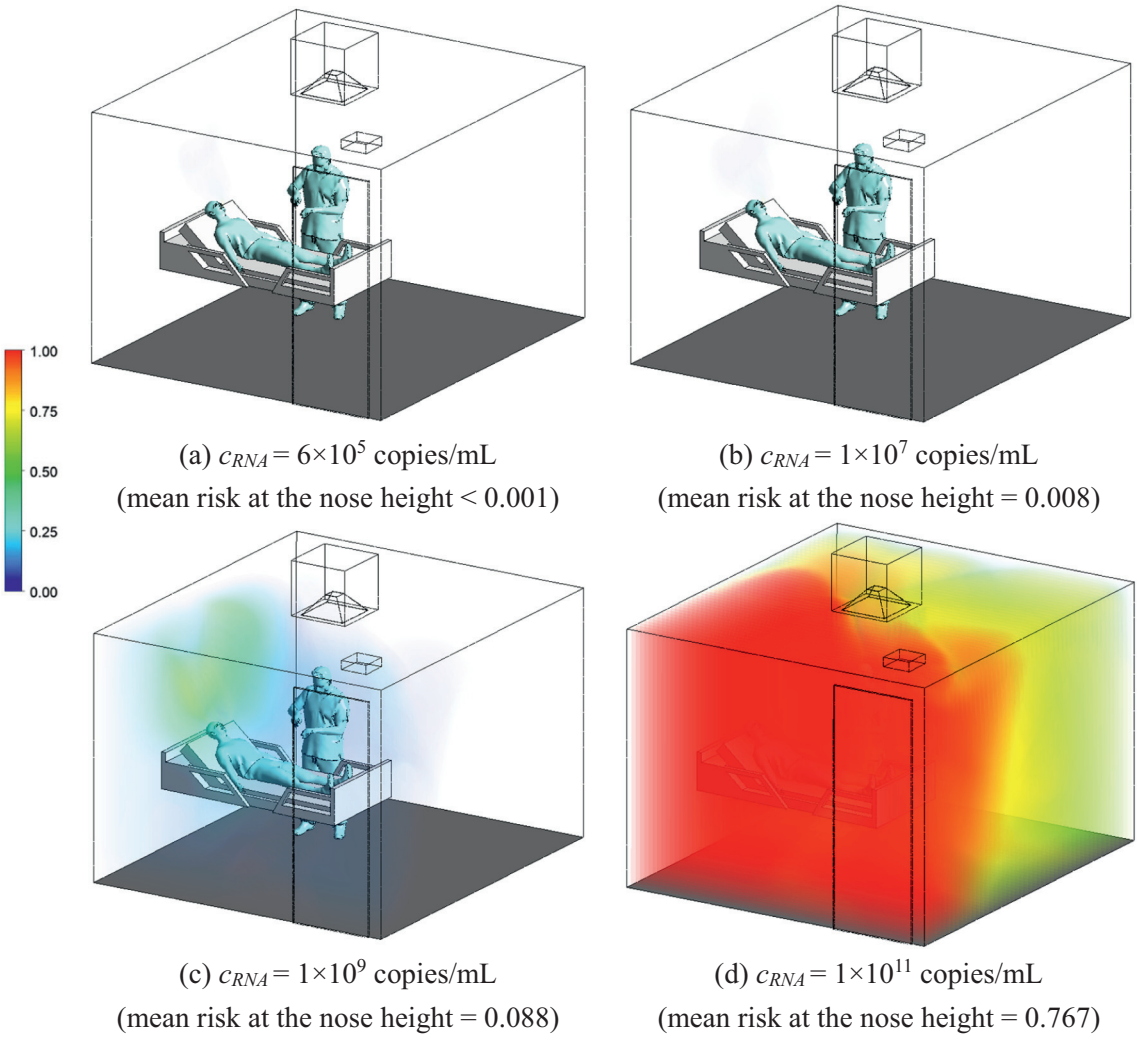

Fig. 9. Effects of the viral load on the infection risk ($\eta_I = 0$, $\eta_S = 0.715$, $TCID_{50} = 10^4$ virions, $t_e = 3600$ s). The results show that viral load is another important variable affecting the transmissibility of the virus.

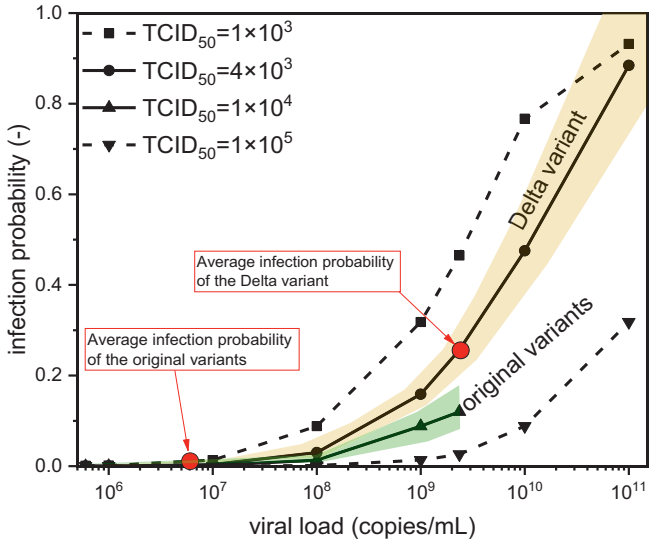

Fig. 10. Infection risk as a function of viral load and $TCID_{50}$ value for 1 h exposure in patient room 3 ($\eta_I = 0$, $\eta_S = 0.715$, $t_e = 3600$ s). On average, the Delta variant is predicted to be around 200 times more contagious than the original variants.

surgical masks can only provide effective protection under very low aerosol concentration and viral load conditions (Fig. 12(d)). As the viral load exceeds 10^9 copies/mL, the efficacy of surgical masks is very limited (Fig. 12(b) and (e)). If the viral load further increases, N95 respirators will lose their high level of protection too, as shown in Fig. 12(c) and (f).

The computations clearly demonstrate the benefits for both the infected and susceptible person to properly wear respiratory PPE. However, respiratory PPE is effective only when the viral load is low and $TCID_{50}$ is large. At high viral loads and small $TCID_{50}$ units, respiratory PPE can only provide very limited protection. In fact, PPE locates at the bottom of the NIOSH's hierarchy of hazard controls (NIOSH, 2015), meaning it is the least effective method for hazard control. As highly contagious variants such as the Delta (Scudellari, 2021) and Lambda (Kimura et al., 2021) variants are increasingly causing concerns all over the world, more effective protection strategies must be developed.

3.5. Infection risk in the common ward area

In this subsection we determine the infection risk in common ward area arising from infectious patients in the ward rooms. To achieve this, the predicted air and aerosol mass flow rates at the door gap of the patient room are extracted and applied as boundary conditions for

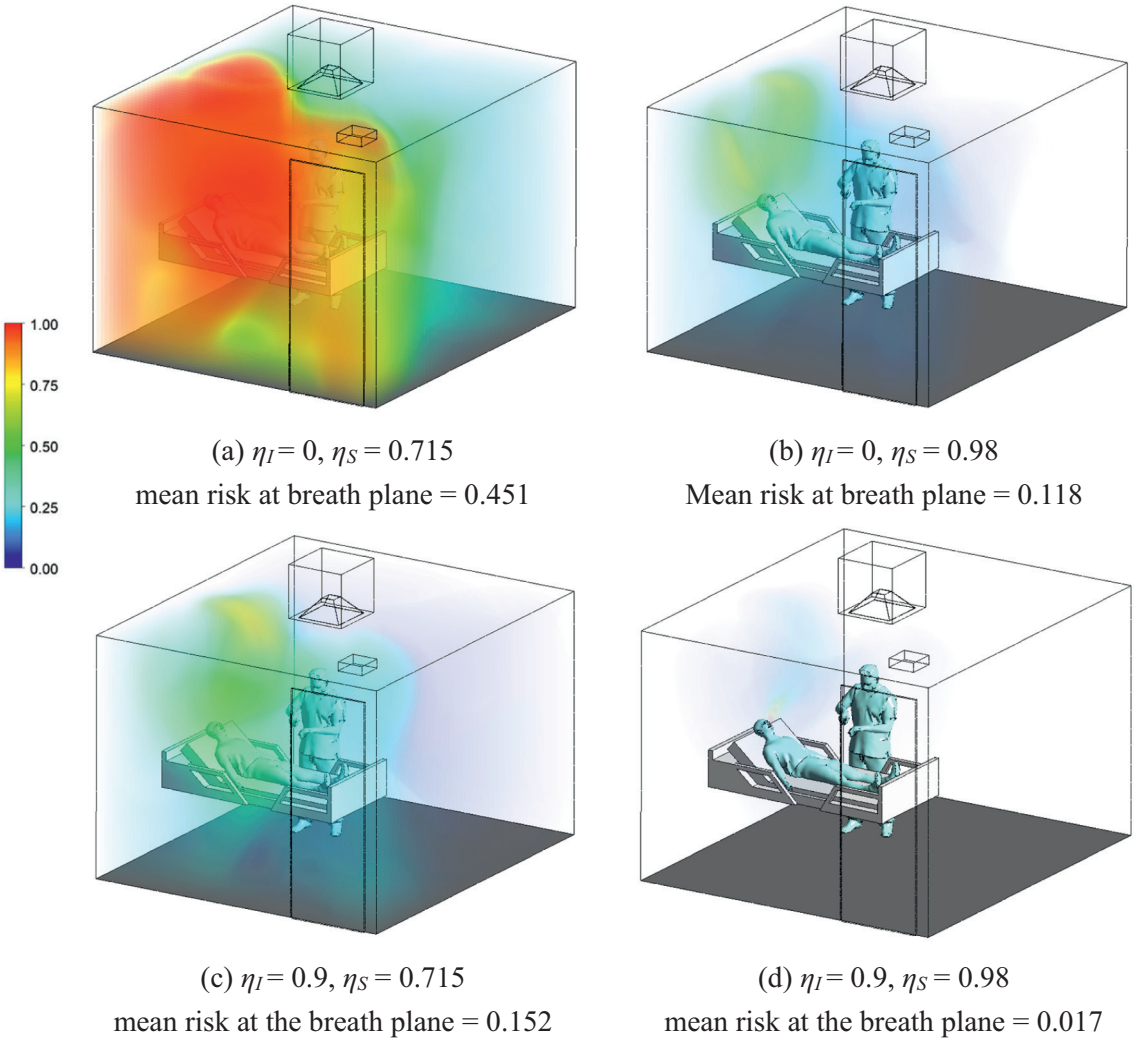

Fig. 11. Effects of PPE on infection risk ($c_{RNA} = 8.82 \times 10^9$ copies/mL, $TCID_{50} = 4000$ virions, $t_e = 3600$ s). The results clearly demonstrate the benefits for both the infected and susceptible persons to wearing a mask.

the CFD model of the common ward area. CFD computations are completed with the exposure time ranging from 10 min to 8 h, representing the shortest and longest possible time that a staff member may stay in the work area. Other computational parameters include transmissivity for the Delta variant of $TCID_{50} = 4000$ and $c_{RNA} = 8.82 \times 10^9$ copies/mL (Li et al., 2021a). All the susceptible persons are wearing a N95 respirator ($\eta_S = 0.98$).

The air flow field in the horizontal plane at the nose height (H = 1.65 m) and 3D particle concentration field in the work area are shown in Fig. 13. The computations predict an evenly distributed air flow field with an average air speed of 0.11 m/s. Local high-speed regions can be seen near the door gaps and ventilation diffusers (Fig. 13 (a)). It also can be seen that the aerosol that escapes from the patient rooms is carried by the ventilation air flow, creating a heterogeneous particle concentration field. Relatively high-concentration regions are observed in the corridor close to Patient Rooms 1 and 2 (Fig. 13(b)) where two room doors are close to each other, and fresh air is not directly supplied to. Compared to that in the patient rooms (Fig. 7), the aerosol concentration in the work area is around 2 orders of magnitude lower. The spatial distribution of airborne infection risk over an 8-hour duration in the common ward area is shown in Fig. 13(c). Similar to the aerosol concentration field, the spatial infection risk distribution is highly heterogeneous throughout the common ward area.

The mean infection risk in the horizontal plane at the breathing height (H = 1.65 m) in the common ward area is calculated using different values of exposure time t_e and viral load c_{RNA}, as shown in Fig. 14. As expected, the infection risk increases with the exposure time as per the exponential decay in (11). For SARS-CoV-2 variants with low viral loads such as the original variants with a mean viral load of $c_{RNA} = 7 \times 10^6$ copies/mL, the infection risk over an 8-hour duration in the work area is negligible if high-efficiency respiratory PPE (e.g., N95 respirators) is properly worn by the susceptible persons. However, for variants with high viral loads such as the Delta variant, the mean 8-hour infection risk dramatically increases to 0.02 even if 90% of the aerosol particles exhaled by the infected persons in the patient rooms are filtered out ($\eta_I = 0.9$) using facial masks. If the infected persons are not wearing masks, the mean infection risk can be as high as 0.177.

The computations show that although the infection risk in the work area is significantly lower than that in the patient rooms, it is still high for an 8-hour exposure if the virus has a small $TCID_{50}$ unit or can produce a high viral load, as is the case for the Delta variant (Li et al., 2021a). In these circumstances, conventional respiratory PPE such as surgical masks and N95 respirators are not able to provide effective protection. Although Figs. 12 and 14 clearly demonstrate that reducing aerosol emission and/or inhalation via respiratory PPE is an effective approach to lowered infection risk, further improvement of the

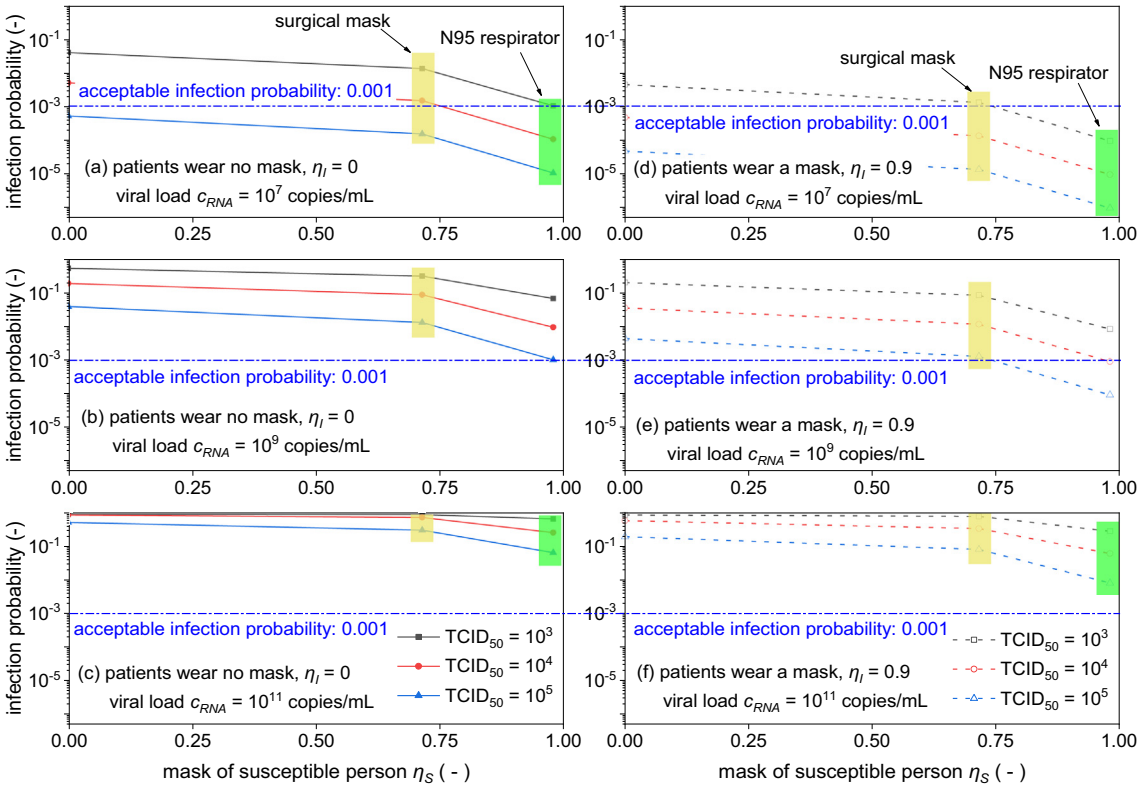

Fig. 12. Effects of respiratory PPE (HID$_{50}$ = 5 × TCID$_{50}$ = 20,000 virions, t_e = 3600 s). The results suggest that respiratory PPE can provide good protection when the viral load is low. However, additional protections are needed if the viral load is high.

filtration efficiency of masks mat not be possible. From Eq. (7), the ratio (δ) of HID$_{50}$ to TCID$_{50}$ is correlated to the level of immunisation. An elevated vaccination level increases δ and hence reduces infection probability. This is important for the development of efficient strategies to fight the COVID-19 pandemic (Priesemann et al., 2021). In addition, engineering controls such as optimal ventilation design can significantly reduce exposure to airborne pathogens in indoor environments. However, many contemporary buildings including healthcare facilities adopt a mixing ventilation scheme, which enhances the mixing of air and so promotes spread of COVID-19 in the indoor environment. This issue has been identified by many investigators (Lepore et al., 2021; Li et al., 2021b; Sodiq et al., 2021) and in public media. Melikov (2020) suggests that to fight COVID-19, we need a paradigm shift in ventilation design. This issue of ventilation optimisation shall be topic of future research, and the spatiotemporal Wells-Riley model developed herein is well suited to the development of such mitigation strategies.

4. Conclusions

A novel spatiotemporal Wells-Riley model for airborne disease transmission risk is developed based on the clinical data of viral shedding by COVID-19 patients and biomedical data of SARS-CoV-2 virions infecting human cells. This model utilises multiphase computational fluid dynamics (CFD) modelling of aerosol transport, forming an integrated predictive framework for spatiotemporal resolution of SARS-CoV-2 infection risks in ventilated indoor environment. This general framework can resolve the impact of many factors upon airborne SARS-CoV-2 transmission risk including SARS-CoV-2 variant and illness time of infected persons, level and type of vaccination of susceptible persons, level and type of PPE worn by infected and/or susceptible persons, location and movement of infected and/or susceptible persons in indoor environment, and natural and mechanised ventilation. The predictive model is applied to a hospital ward accommodating COVID-19 patients and computations are performed under a range of assumed scenarios. Conclusions rising from this study are as follows:

(1) The new predictive model provides a comprehensive method to predict the infection risk associated with the exposure to airborne pathogens including SARS-CoV-2. The characteristics of different SARS-CoC-2 variants, immunisation level of and donning of respiratory PPE by the occupants, as well as the ventilation setup can be holistically considered in a single model. The model provides a comprehensive theoretical framework, for the first time, to integrate clinical data, biomedical data and engineering designs in a single predictive model, and has enabled quantitative, spatial-temporal analysis of COVID-19 transmission in indoor environment.

(2) This study highlights the significance of wearing respiratory PPE by both the infected and susceptible persons. Respiratory PPE can provide very good protection when the viral load is low and the variant is not very contagious. However, with an increasing viral load and/or smaller TCID$_{50}$ unit, the efficacy of respiratory PPE quickly decreases. For highly contagious variants such as the Delta variant, respiratory PPE can only provide very limited protection in healthcare settings. As highly contagious variants of SARS-CoV-2 are increasingly causing concerns all over the world, a paradigm shift in ventilation and improved level of vaccination is needed to reduce the risk in high-risk environments.

CRediT authorship contribution statement

Xiangdong Li: Conceptualization, Investigation, Methodology, Numerical computation, Writing – original draft. **Daniel Lester**: Conceptualisation, Methodology, Writing – review and editing. **Gary Rosengarten**: Conceptualisation, Writing – review and editing. **Craig Aboltins**: Clinical and epidemiological data curation, Writing – review and editing. **Milan**

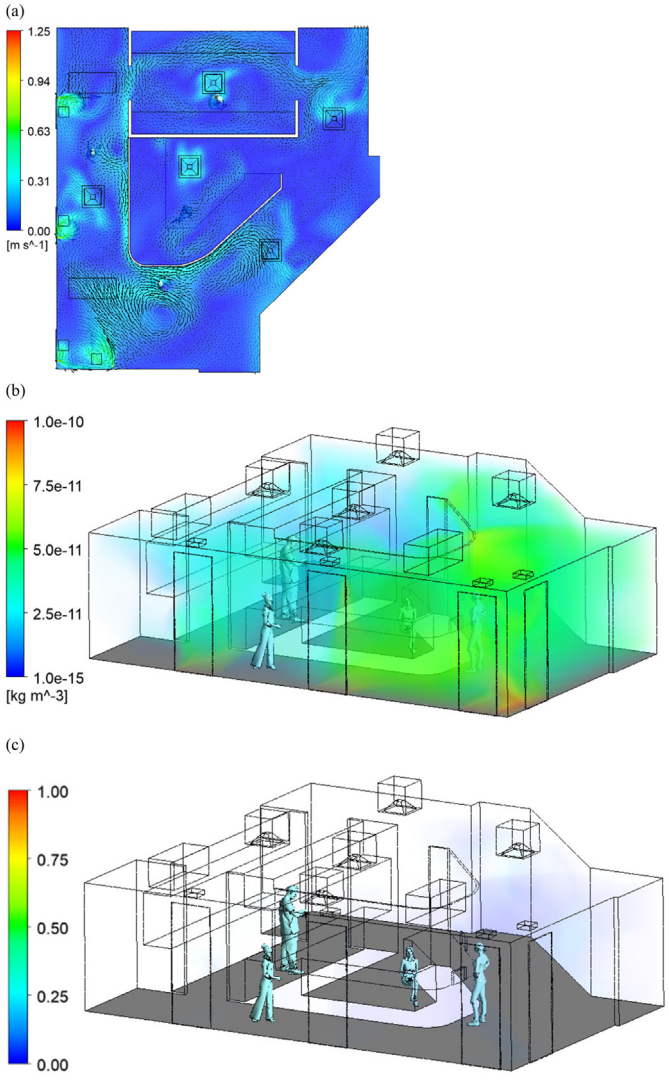

Fig. 13. CFD results of the common ward area ($TCID_{50}$ = 4000 virions, c_{RNA} = 8.82 × 10^9 copies/mL, t_e = 8 h, η_I = 0.9, η_S = 0.98). The computations show highly heterogeneous distributions of aerosol and infection risk in the ward. (a) Air flow field at H = 1.65 m. (b) Particle concentration field. (c) Spatial distribution of infection risk.

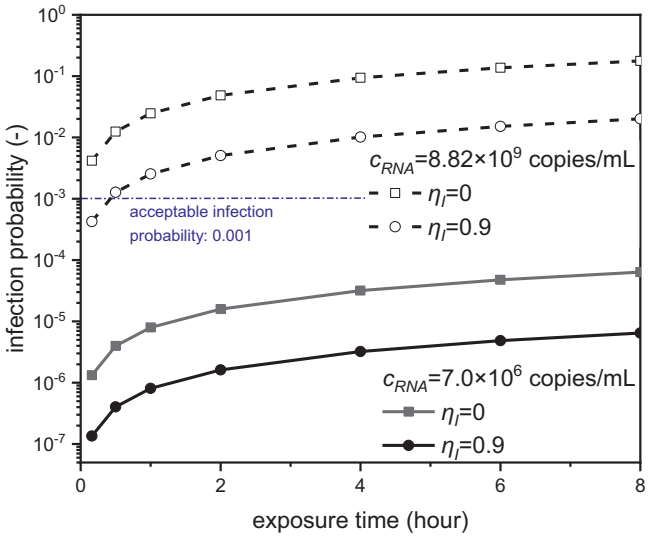

Fig. 14. Effects of viral load and exposure time on the infection probability (η_S = 0.98) outside the patient rooms at a noise height of H = 1.65 m.

Patel: Project administration, Resources, Writing – review and editing. **Ivan Cole**: Funding acquisition, Supervision, Writing – review and editing.

Declaration of competing interest

The authors declare that they have no known competing financial interests or personal relationships that could have appeared to influence the work reported in this paper.

Acknowledgement

The authors gratefully acknowledge funding from RMIT University through the Restart Initiative and Enabling Capability Platforms and the Victorian Government through its Victorian Higher Education State Investment Fund Pool A.

Appendix A. Supplementary data

Supplementary data to this article can be found online at https://doi.org/10.1016/j.scitotenv.2021.152592.

References

ANSI, 2004. Thermal Environmental Conditions for Human Occupancy. vol. 55. American Society of Heating, Refrigerating and Air-Conditioning Engineers.

Bar-On, Y.M., Flamholz, A., Phillips, R., Milo, R., 2020. SARS-CoV-2 (COVID-19) by the numbers. eLife 9, e57309.

Carroll, R.G., 2007. 10 - pulmonary system. In: Carroll, R.G. (Ed.), Elsevier's Integrated Physiology. Mosby, Philadelphia, pp. 99–115.

Chao, C.Y.H., Wan, M.P., Morawska, L., Johnson, G.R., Ristovski, Z.D., Hargreaves, M., et al., 2009. Characterization of expiration air jets and droplet size distributions immediately at the mouth opening. J. Aerosol Sci. 40, 122–133.

Chen, F., Yu, S.C.M., Lai, A.C.K., 2006. Modeling particle distribution and deposition in indoor environments with a new drift–flux model. Atmos. Environ. 40, 357–367.

Chirico, F., Sacco, A., Bragazzi, N.L., Magnavita, N., 2020. Can air-conditioning systems contribute to the spread of SARS/MERS/COVID-19 Infection? Insights from a rapid review of the literature. Int. J. Environ. Res. Public Health 17.

Chong, K.L., Ng, C.S., Hori, N., Yang, R., Verzicco, R., Lohse, D., 2021. Extended lifetime of respiratory droplets in a turbulent vapor puff and its implications on airborne disease transmission. Phys. Rev. Lett. 126, 034502.

Clapp, P.W., Sickbert-Bennett, E.E., Samet, J.M., Berntsen, J., Zeman, K.L., Anderson, D.J., et al., 2021. Evaluation of cloth masks and modified procedure masks as personal protective equipment for the public during the COVID-19 pandemic. JAMA Intern. Med. 181, 463–469.

de Dear, R.J., Arens, E., Hui, Z., Oguro, M., 1997. Convective and radiative heat transfer coefficients for individual human body segments. Int. J. Biometeorol. 40, 141–156.

Evrard, F., Denner, F., van Wachem, B., 2021. Quantifying the errors of the particle-source-in-cell Euler-Lagrange method. Int. J. Multiphase Flow 135, 103535.

Fisk, W., Seppanen, O., Faulkner, D., Huang, J., 2005. Economic benefits of an economizer system: energy savings and reduced sick leave. ASHRAE Trans. 111.

Gosak, M., Duh, M., Markovič, R., Perc, M., 2021. Community lockdowns in social networks hardly mitigate epidemic spreading. New J. Phys. 23, 043039.

Greenhalgh, T., Jimenez, J.L., Prather, K.A., Tufekci, Z., Fisman, D., Schooley, R., 2021. Ten scientific reasons in support of airborne transmission of SARS-CoV-2. Lancet 397, 1603–1605.

Inthavong, K., Ge, Q.J., Li, X.D., Tu, J.Y., 2013. Source and trajectories of inhaled particles from a surrounding environment and its deposition in the respiratory airway. Inhal. Toxicol. 25, 280–291.

Iwami, S., Holder, B.P., Beauchemin, C.A.A., Morita, S., Tada, T., Sato, K., et al., 2012. Quantification system for the viral dynamics of a highly pathogenic simian/human immunodeficiency virus based on an in vitro experiment and a mathematical model. Retrovirology 9, 18.

Kenarkoohi, A., Noorimotlagh, Z., Falahi, S., Amarloei, A., Mirzaee, S.A., Pakzad, I., et al., 2020. Hospital indoor air quality monitoring for the detection of SARS-CoV-2 (COVID-19) virus. Sci. Total Environ. 748, 141324.

Kimura, I., Kosugi, Y., Wu, J., Yamasoba, D., Butlertanaka, E.P., Tanaka, Y.L., et al., 2021. SARS-CoV-2 Lambda Variant Exhibits Higher Infectivity and Immune Resistance. bioRxiv 2021.07.28.454085.

Kwon, K.S., Park, J.I., Park, Y.J., Jung, D.M., Ryu, K.W., Lee, J.H., 2020. Evidence of long-distance droplet transmission of SARS-CoV-2 by direct air flow in a restaurant in Korea. J. Korean Med. Sci. 35, e415.

Lepore, E., Aguilera Benito, P., Piña Ramírez, C., Viccione, G., 2021. Indoors ventilation in times of confinement by SARS-CoV-2 epidemic: a comparative approach between Spain and Italy. Sustain. Cities Soc. 72, 103051.

Li, X.D., Zhang, H., Wang, R.S., Wang, J., 2010. MUSIG modeling and evaluation of nitrogen bubble coalescence in a bottom-closed vertical tube. Aerosp. Sci. Technol. 14, 203–212.

Li, X., Yan, Y., Shang, Y., Tu, J., 2015. An Eulerian-Eulerian model for particulate matter transport in indoor spaces. Build. Environ. 86, 191–202.
Li, X., Shang, Y., Yan, Y., Yang, L., Tu, J., 2018. Modelling of evaporation of cough droplets in inhomogeneous humidity fields using the multi-component Eulerian-Lagrangian approach. Build. Environ. 128, 68–76.
Li, B., Deng, A., Li, K., Hu, Y., Li, Z., Xiong, Q., et al., 2021a. Viral Infection and Transmission in a Large Well-traced Outbreak Caused by the Delta SARS-CoV-2 Variant. medRxiv 2021.07.07.21260122.
Li, Y., Qian, H., Hang, J., Chen, X., Cheng, P., Ling, H., et al., 2021b. Probable airborne transmission of SARS-CoV-2 in a poorly ventilated restaurant. Build. Environ. 196, 107788.
Liotti, F.M., Menchinelli, G., Lalle, E., Palucci, I., Marchetti, S., Colavita, F., et al., 2021. Performance of a novel diagnostic assay for rapid SARS-CoV-2 antigen detection in nasopharynx samples. Clin. Microbiol. Infect. 27, 487–488.
Liu, Z., Zhuang, W., Hu, X., Zhao, Z., Rong, R., Li, J., et al., 2021. Potential infection risk assessment of improper bioaerosol experiment operation in one BSL-3 laboratory based on the improved Wells-Riley method. Build. Environ. 201, 107974.
Ma, S., Li, H., Yang, J., Yu, K., 2021. Molecular simulation studies of the interactions between the human/pangolin/cat/bat ACE2 and the receptor binding domain of the SARS-CoV-2 spike protein. Biochimie 187, 1–13.
Markovič, R., Šterk, M., Marhl, M., Perc, M., Gosak, M., 2021. Socio-demographic and health factors drive the epidemic progression and should guide vaccination strategies for best COVID-19 containment. Results Phys. 26, 104433.
Melikov, A.K., 2020. COVID-19: reduction of airborne transmission needs paradigm shift in ventilation. Build. Environ. 186, 107336.
Mikko, M., Taivassalo, V., Kallio, S., 1996. On the Mixture Model for Multiphase Flow. 288. VTT Publications.
Miller, S.L., Nazaroff, W.W., Jimenez, J.L., Boerstra, A., Buonanno, G., Dancer, S.J., et al., 2021. Transmission of SARS-CoV-2 by inhalation of respiratory aerosol in the Skagit Valley chorale superspreading event. Indoor Air 31, 314–323.
Nicas, M., Nazaroff, W.W., Hubbard, A., 2005. Toward understanding the risk of secondary airborne infection: emission of respirable pathogens. J. Occup. Environ. Hyg. 2, 143–154.
Nikitin, N., Petrova, E., Trifonova, E., Karpova, O., 2014. Influenza virus aerosols in the air and their infectiousness. Adv. Virol. 2014, 859090.
NIOSH, 2015. Hierarchy of Controls. 2021. National Institute for Occupational Safety and Health National Institute for Occupational Safety and Health (NIOSH).
Noorimotlagh, Z., Jaafarzadeh, N., Martínez, S.S., Mirzaee, S.A., 2021. A systematic review of possible airborne transmission of the COVID-19 virus (SARS-CoV-2) in the indoor air environment. Environ. Res. 193, 110612.
Parker, J., Fowler, N., Walmsley, M.L., Schmidt, T., Scharrer, J., Kowaleski, J., et al., 2015. Analytical sensitivity comparison between singleplex real-time PCR and a multiplex PCR platform for detecting respiratory viruses. PLoS One 10, e0143164.
Pollock, N.R., Savage, T.J., Wardell, H., Lee, R.A., Mathew, A., Stengelin, M., et al., 2021. Correlation of SARS-CoV-2 nucleocapsid antigen and RNA concentrations in nasopharyngeal samples from children and adults using an ultrasensitive and quantitative antigen assay. J. Clin. Microbiol. 59.
Priesemann, V., Balling, R., Bauer, S., Beutels, P., Valdez, A.C., Cuschieri, S., et al., 2021. Towards a European strategy to address the COVID-19 pandemic. Lancet 398, 838–839.
Riley, E.C., Murphy, G., Riley, R.L., 1978. Airborne spread of measles in a suburban elementary school. Am. J. Epidemiol. 107, 421–432.
Scheepers, C., Everatt, J., Amoako, D.G., Mnguni, A., Ismail, A., Mahlangu, B., et al., 2021. The Continuous Evolution of SARS-CoV-2 in South Africa: A New Lineage With Rapid Accumulation of Mutations of Concern and Global Detection. medRxiv 2021.08.20.21262342.
Scudellari, M., 2021. How the coronavirus infects cells - and why Delta is so dangerous. Nature 595, 640–644.
Sehrawat, S., Rouse, B.T., 2021. COVID-19: disease, or no disease? - that is the question. It's the dose stupid! Microbes Infect. 23, 104779.
Sender, R., Bar-On, Y.M., Gleizer, S., Bernshtein, B., Flamholz, A., Phillips, R., et al., 2021. The total number and mass of SARS-CoV-2 virions. Proc. Natl. Acad. Sci. 118, e2024815118.
Shen, J., Kong, M., Dong, B., Birnkrant, M.J., Zhang, J., 2021. A systematic approach to estimating the effectiveness of multi-scale IAQ strategies for reducing the risk of airborne infection of SARS-CoV-2. Build. Environ. 200, 107926.
Sodiq, A., Khan, M.A., Naas, M., Amhamed, A., 2021. Addressing COVID-19 contagion through the HVAC systems by reviewing indoor airborne nature of infectious microbes: will an innovative air recirculation concept provide a practical solution? Environ. Res. 199, 111329.
Srivastava, S., Zhao, X., Manay, A., Chen, Q., 2021. Effective ventilation and air disinfection system for reducing coronavirus disease 2019 (COVID-19) infection risk in office buildings. Sustain. Cities Soc. 75, 103408.
Stadnytskyi, V., Bax, C.E., Bax, A., Anfinrud, P., 2020. The airborne lifetime of small speech droplets and their potential importance in SARS-CoV-2 transmission. Proc. Natl. Acad. Sci. 117, 11875–11877.
Sze To, G.N., Chao, C.Y., 2010. Review and comparison between the Wells-Riley and dose-response approaches to risk assessment of infectious respiratory diseases. Indoor Air 20, 2–16.
Tang, J.W., Bahnfleth, W.P., Bluyssen, P.M., Buonanno, G., Jimenez, J.L., Kurnitski, J., et al., 2021. Dismantling myths on the airborne transmission of severe acute respiratory syndrome coronavirus-2 (SARS-CoV-2). J. Hosp. Infect. 110, 89–96.
van Doremalen, N., Bushmaker, T., Morris, D.H., Holbrook, M.G., Gamble, A., Williamson, B.N., et al., 2020. Aerosol and surface stability of SARS-CoV-2 as compared with SARS-CoV-1. N. Engl. J. Med. 382, 1564–1567.
Villafruela, J.M., San José, J.F., Castro, F., Zarzuelo, A., 2016. Airflow patterns through a sliding door during opening and foot traffic in operating rooms. Build. Environ. 109, 190–198.
Villermaux, E., Moutte, A., Amielh, M., Meunier, P., 2017. Fine structure of the vapor field in evaporating dense sprays. Phys. Rev. Fluids 2.
Wells, W.F., 1955. Airborne contagion and air hygiene: an ecological study of droplet infections. J. Am. Med. Assoc. 159, 90.
Wölfel, R., Corman, V.M., Guggemos, W., Seilmaier, M., Zange, S., Müller, M.A., et al., 2020. Virological assessment of hospitalized patients with COVID-2019. Nature 581, 465–469.
Yan, Y., Li, X., Shang, Y., Tu, J., 2017. Evaluation of airborne disease infection risks in an airliner cabin using the Lagrangian-based Wells-Riley approach. Build. Environ. 121, 79–92.
Yan, A.W.C., Zaloumis, S.G., Simpson, J.A., McCaw, J.M., 2019a. Sequential infection experiments for quantifying innate and adaptive immunity during influenza infection. PLoS Comput. Biol. 15, e1006568.
Yan, Y., Li, X., Tu, J., 2019b. Thermal effect of human body on cough droplets evaporation and dispersion in an enclosed space. Build. Environ. 148, 96–106.
Yu, A., Pak, A.J., He, P., Monje-Galvan, V., Casalino, L., Gaieb, Z., et al., 2021. A multiscale coarse-grained model of the SARS-CoV-2 virion. Biophys. J. 120, 1097–1104.
Yuan, Y., Li, X., Tu, J., 2016. Numerical modelling of air–nanofluid bubbly flows in a vertical tube using the MUltiple-SIze-Group (MUSIG) model. Int. J. Heat Mass Transf. 102, 856–866.
Zhang, Z., Chen, Q., 2007. Comparison of the eulerian and lagrangian methods for predicting particle transport in enclosed spaces. Atmos. Environ. 41, 5236–5248.
Zhang, S., Lin, Z., 2021. Dilution-based evaluation of airborne infection risk - thorough expansion of Wells-Riley model. Build. Environ. 194, 107674.
Zhang, R., Li, Y., Zhang, A.L., Wang, Y., Molina, M.J., 2020. Identifying airborne transmission as the dominant route for the spread of COVID-19. Proc. Natl. Acad. Sci. 117, 14857–14863.